Applied Catalysis B: Environmental 202 (2017) 84–94

Contents lists available at ScienceDirect

Applied Catalysis B: Environmental

journal homepage: www.elsevier.com/locate/apcatb

Ultra-low loading of Ag_3PO_4 on hierarchical In_2S_3 microspheres to improve the photocatalytic performance: The cocatalytic effect of Ag and Ag_3PO_4

Tingjiang Yan[a,b,*], Jun Tian[a], Wenfei Guan[a], Zheng Qiao[a], Wenjuan Li[a], Jinmao You[a], Baibiao Huang[b,**]

[a] The Key Laboratory of Life-Organic Analysis, College of Chemistry and Chemical Engineering, Qufu Normal University, Qufu, Shandong 273165, PR China
[b] State Key Laboratory of Crystal Materials, Shandong University, Jinan, Shandong 250100, PR China

ARTICLE INFO

Article history:
Received 23 June 2016
Received in revised form 31 July 2016
Accepted 6 September 2016
Available online 6 September 2016

Keywords:
Ag_3PO_4
In_2S_3
cocatalyst
ultra–low
photocatalysis

ABSTRACT

Ag_3PO_4/In_2S_3 composite photocatalysts with ultra–low loading of Ag_3PO_4 (0.017 ~ 4.89 wt %) were prepared by a facile precipitate method and characterized by XRD, SEM, TEM, HRTEM, BET, DRS and XPS techniques. The as–obtained composites were employed to degrade different kinds of organic pollutants (dyes and colorless pollutants) in aqueous solution under visible light irradiation. The Ag_3PO_4/In_2S_3 composites exhibited excellent adsorption capacity and photocatalytic activity. The optimal composite with 0.086 wt % Ag_3PO_4 content exhibited the highest photocatalytic activity, which could degrade almost all dyes (MO, MB and RhB) within 7 min of light irradiation and more than 50% of phenol and salicylic acid after 3 h of irradiation. Recycling experiments confirmed that the Ag_3PO_4/In_2S_3 catalysts had superior cycle performance and structural stability. The photocatalytic activity enhancement of Ag_3PO_4/In_2S_3 composites could be mainly attributed to the efficient separation of photogenerated charge carriers through a Z–scheme system composed of Ag_3PO_4, Ag and In_2S_3, in which Ag nanoparticles acted as the charge transmission bridge. The high photocatalytic stability was ascribed to the successful inhibition of the photocorrsion of both In_2S_3 and Ag_3PO_4 by transferring the photogenerated holes and electrons from them to Ag, respectively. This study indicated the application of Ag–Ag_3PO_4 as cocatalyst and provided a new way to design and prepare high–efficiency and stable photocatalysts for photocatalytic decontamination of organic pollutants.

1. Introduction

Semiconductor photocatalysis has been considered as an effective and most promising strategy to address the environmental crises and energy shortage issues [1,2]. In view of the efficient utilization of solar energy, numerous attempts have been made in recent years to develop different visible light–active photocatalysts. Among them, sulfide photocatalysts including binary sulfides (e.g., CdS, In_2S_3, SnS_2, Cu_2S) and ternary chalcogenides (e.g., $ZnIn_2S_4$, $CdIn_2S_4$, $SnIn_4S_8$) with narrow band gaps, have been proved to be good candidates for photocatalytic hydrogen evolution from water and photocatalytic degradation of organic pollutants under visible light irradiation [3–9]. However, these sulfide photocatalysts are still facing the same challenges encountered by most photocatalysts, such as limited photocatalytic efficiency associated with the fast recombination rate of photogenerated electron–hole pairs and photocorrsion issue due to the oxidation of S–metal bond by photogenerated holes. Traditionally, for improving the photocatalytic efficiency of sulfide photocatalysts, cocatalysts are usually involved to load on base photocatalysts. The introduction of cocatalysts not only effectively separates the electron–hole pairs but also provides more active sites to facilitate the adsorption and oxidation/reduction reactions. For instance, Zong et al. reported the enhancement of photocatalytic H_2 evolution on CdS by loading MoS_2 or WS_2 as cocatalyst under visible light irradiation [10,11]. Shen and co-workers observed that dual cocatalysts consisting of noble metals (Pt) and transition-metal sulfides (Ag_2S, SnS, CuS) played a crucial role in achieving very high efficiency for H_2 evolution over $ZnIn_2S_4$ photocatalyst [12]. Although

* Corresponding author at: The Key Laboratory of Life-Organic Analysis, College of Chemistry and Chemical Engineering, Qufu Normal University, Qufu, Shandong, 273165, PR China.
** Corresponding author.
E-mail addresses: tingjiangn@163.com (T. Yan), bbhuang@sdu.edu.cn (B. Huang).

http://dx.doi.org/10.1016/j.apcatb.2016.09.017
0926-3373/

many other cocatalysts such as $Co(OH)_2$ and graphene oxide have been explored and found to be effective for facilitating the activity of sulfide photocatalysts [13,14], the development of novel cocatalysts to fulfill the high photocatalytic activity is still concerned.

On the other hand, fabrication of heterogeneous–type photocatalytic system is an effective strategy to suppress the photocorrsion because it allows the prompt migration of photogenerated charges [15]. Silver phosphate (Ag_3PO_4) has been reported as a promising photocatalyst with wonderful photocatalytic activity under visible light irradiation since the pioneer work by Ye et al. in 2010 [16]. Due to the outstanding photosensitive and photocatalytic characteristics, Ag_3PO_4 photocatalysts have afterward be used to fabricate heterogeneous composite photocatalysts such as $Ag_3PO_4/In(OH)_3$ [17], AgX/Ag_3PO_4 (X = Cl, Br, I) [18], $SrTiO_3/Ag_3PO_4$ [19], Ag_3PO_4/TiO_2 [20], $Ag_3PO_4/g–C_3N_4$ [21,22], Ag_3PO_4/WS_2 [23], Ag_3PO_4/MoS_2 [24], $Ag_3PO_4/InVO_4/BiVO_4$ [25], and so on, in which the photogenerated electron–hole pairs can be separated effectively and the photocatalytic activity and stability of separate component is highly improved. However, the above studies have mainly focused on fabricating Ag_3PO_4–based composite photocatalysts, in which precious Ag_3PO_4 takes up the major component, to some extent restricting the practical use of such heterogeneous photocatalysts. Our recent study reported a low–cost and efficient Ag_3PO_4/SiO_2 complex photocatalytic system by grafting few Ag_3PO_4 photocatalysts onto inexpensive SiO_2 supporting material [26]. An improved photocatalytic activity could be achieved for the decomposition of methyl orange (MO) under visible light irradiation even when the Ag_3PO_4 content decreased to 15 wt% in the Ag_3PO_4/SiO_2 composite photocatalysts.

For the purpose of further decreasing the Ag_3PO_4 content and designing novel high–efficiency and stable photocatalysts, in this study, Ag_3PO_4 as a novel cocatalyst with ultra–low loading amount (0.017–4.89 wt %) was anchored onto In_2S_3 hierarchical microspheres to synthesize Ag_3PO_4/In_2S_3 composites. The photocatalytic performance was evaluated by the degradation of dyes and colorless organic pollutants under visible light irradiation. The Ag_3PO_4/In_2S_3 composites exhibited excellent photocatalytic activity and stability. The reaction mechanism of the improved photocatalytic performance of Ag_3PO_4/In_2S_3 composites was also investigated. This work may provide new insights for the design and preparation of new high–efficiency and stable visible–light–driven photocatalysts.

2. Experimental Section

2.1. Materials

All of the reagents used in this experiment were analytical reagent grade and without further purification. Indium chloride tetrahydrate ($InCl_3·4H_2O$), L–cysteine, sodium hydroxide (NaOH), disodium hydrogen phosphate ($Na_2HPO_4·12H_2O$), silver nitrate ($AgNO_3$), commercial Al_2O_3, methyl orange (MO), nitroblue tetrazolium (NBT) and ethanol were purchased from Sinopharm Chemical Reagent Co. Ltd. Deionized water was used throughout the work.

2.2. Sample preparation

2.2.1. Synthesis of pure In_2S_3

Pure In_2S_3, with a typical flowerlike structure, was synthesized by a hydrothermal method. In a typical synthesis, 0.5 mmol $InCl_3·4H_2O$ and 2 mmol L–cysteine were firstly dissolved in 80 mL of distilled water to form a homogeneous solution under constant vigorous stirring. The pH of the solution was adjusted to 8 by dropwise addition of a 1 M solution of NaOH. After further stirring for 30 min, the resulting solution was transferred into a Teflon–lined stainless autoclave and then heated at 180 °C for 10 h. The obtained products were washed several times with water and ethanol, and the yellow precipitate was dried in an oven at 60 °C. $ZnIn_2S_4$ hierarchical microspheres were synthesized by a similar hydrothermal method.

2.2.2. Synthesis of Ag_3PO_4/In_2S_3 composite

For preparation Ag_3PO_4/In_2S_3 composite photocatalysts, 0.1 g of In_2S_3 powder was dispersed in a set volume of Na_2HPO_4 solution (0.1 M) and ultrasonicated for 0.5 h. A certain amount of $AgNO_3$ solution was then dropped into the solution under vigorous stirring. After stirring for 1 h, the resulting solid product was collected by centrifugation, washed with distilled water, and dried in an oven at 60 °C. In this manner, different weight contents (0.017∼4.89 wt%) of Ag_3PO_4 in Ag_3PO_4/In_2S_3 composite samples were obtained and denoted as AI–1, AI–2, AI–3, AI–4, AI–5 and AI–6, respectively. Pure Ag_3PO_4 and Ag_3PO_4/Al_2O_3 samples were respectively prepared using the same procedures as AI–2 except that no In_2S_3 was added and In_2S_3 was replaced by commercial Al_2O_3. Pt/In_2S_3 was synthesized by impregnating the In_2S_3 catalysts with an aqueous H_2PtCl_6 solution followed by reduction using $NaBH_4$ as reduction reagent. The initial ratio of Pt to In_2S_3 was fixed at 0.086 wt %.

2.3. Sample Characterizations

X–ray diffraction patterns (XRD) were collected on a Rigaku MinFlex II equipped with Cu Kα irradiation. The morphology of the samples was investigated with field emission scanning electron microscope (FESEM) (Hitachi SU-8000). The high–resolution transmission electron microscopy (HRTEM) measurement was conducted using a JEM–2010 microscope working at 200 kV. X-ray photoelectron spectroscopy (XPS) analysis was conducted on an ESCALAB 250 photoelectron spectroscope (Thermo Fisher Scientific) at 3.0×10^{-10} mbar with monochromatic Al Kα radiation (E = 1486.2 eV), the binding energy was corrected with reference to the C 1 s peak (284.6 eV) for each sample. BET surface area was performed on an ASAP2020 M apparatus (Micromeritics Instrument Corp., USA). For BET surface area analyses, the samples were degassed in vacuum at 200 °C for 10 h and then measured at 77 K. UV−visible diffuse reflectance spectra (DRS) of the powders were obtained for the dry-pressed disk samples using a Cary 500 Scan Spectrophotometer (Varian, USA) over a range of 200–800 nm. $BaSO_4$ was used as a reflectance standard in the UV−visible diffuse reflectance experiment. The photoluminescence (PL) spectra were obtained by using a F-4600 Fluorescence spectrophotometer with an excitation wavelength of 216 nm. Photoelectrochemical measurements were conducted with an epsilon (BAS) electrochemical workstation. A 300W Xe–arc lamp equipped with cutoff filters (400 nm < λ < 800 nm) was used as a visible light source. A standard three-electrode cell with a work electrode (as-prepared photocatalyst), a platinum wire as counter electrode, and a standard calomel electrode as reference electrode were used in the photoelectric studies. 0.1 M Na_2SO_4 was used as the electrolyte solution. All electrochemical potentials are reported vs. NHE.

2.4. Evaluation of Photocatalytic Activity

Photocatalytic experiments were performed in an aqueous solution at ambient temperature. A 300 W Xe–arc lamp equipped with cutoff filters (400 nm < λ < 800 nm) was used as the visible light source. The system was cooled by a fan and circulating water to maintain at room temperature. Briefly, 80 mg of photocatalyst was suspended in 80 mL dye solution (MO, RhB and MB, 10 ppm), phenol solution (10 ppm) or salicylic acid solution (10 ppm). Prior to irradiation, the suspension was magnetically stirred in dark for 1 h

to establish an adsorption – desorption equilibrium. A 3 mL aliquot was taken at several minutes intervals during the experiment and centrifuged to remove the powders. The residual concentration of dye and salicylic acid was analyzed on a Shanghai Youke UV756CRT spectrophotometer, whereas it for phenol was detected with a P230 high-performance liquid chromatograph. The degradation percentage is reported as C/C_0, where C_0 is the initial concentration of dye, and C represents the corresponding concentration at a certain time interval. The stability was tested as follows: after each dye degradation reaction, the suspension was filtered and the solids were washed with water and dried at 60 °C in air. Then the regenerated product was employed to degrade a new dye aqueous solution for another test under the same visible light irradiation. Total organic carbon (TOC) was measured with a Shimadzu TOC-4100 analyzer.

2.5. Active Species Trapping Experiments

For detecting the active species during photocatalytic process, some sacrificial agents, such as tertbutyl alcohol (TBA), ammonium oxalate (AO) and benzoquinone (BQ) were used as the scavengers of hydroxyl radical (•OH), hole (h^+) and superoxide radical ($•O_2^-$), respectively. The method was similar to the former photocatalytic activity process with the addition of 0.1 mmol/L of quencher in the presence of 80 mL MO (10 ppm). The light illumination time was 7 min.

3. Results and discussion

3.1. Characterization of as-prepared samples

The Ag_3PO_4/In_2S_3 composite photocatalysts were prepared by a two–step route involving the hydrothermal synthesis of In_2S_3 hierarchical microspheres and the loading of small Ag_3PO_4 nanoparticles. The successful preparation of Ag_3PO_4/In_2S_3 composite is highly dependent on the addition sequence of silver ions and phosphate anions. If silver ions were firstly added into In_2S_3 suspension solution, the original yellow solution immediately changed into black solution, regardless of the further introduction of phosphate anions. The XRD and SEM results (Fig. S1 and S2, supporting information) showed the formation of Ag_2S in this process. On the other hand, when phosphate anions were initially introduced into the homogeneous In_2S_3 solution, the phosphate anions would be chemically adsorbed on the surface of the two–dimensional In_2S_3 sheets due to the strong coordination effect between phosphate anions and complex surface typologies [27,28]. After silver ions were added to react with phosphate anions, Ag_3PO_4 crystals nucleated and grew in the micro-environment created by the In_2S_3 hierarchical microspheres.

Table 1
The mass percentage of Ag_3PO_4 in Ag_3PO_4/In_2S_3 composites and the surface area of the samples.

Samples	In_2S_3	AI–1	AI–2	AI–3	AI–4	AI–5	AI–6
Ag_3PO_4 (wt%)	0	0.017	0.086	0.17	0.85	1.69	4.89
Surface area ($m^2\ g^{-1}$)	10.7	30.2	35.2	36.5	20.9	12.7	5.2

The mass percentage of Ag_3PO_4 in the Ag_3PO_4/In_2S_3 composites is shown in Table 1. It is observed that the Ag_3PO_4 content in the composites is ultra–low, even lower than 0.1% in some composites. Taking into account the precious Ag in the composites, the actual content of Ag can be further down to 77%, which shows promising potential application in practical photocatalytic reaction.

Composition and crystallographic structure of pure In_2S_3, Ag_3PO_4 and the as–prepared Ag_3PO_4/In_2S_3 composite photocatalysts were determined by XRD and the results are depicted in Fig. 1. As shown in Fig. 1a, all the diffraction peaks of pure samples can be indexed to the standard diffraction data of the corresponding cubic β–In_2S_3 (JCPDS Card File No. 32-0456) and cubic Ag_3PO_4 (JCPDS Card File No. 06-0505), suggesting the pure phase nature for both samples. The broad diffraction peaks of pure In_2S_3 is attributed to the relatively small crystallite size of the sample [29]. The Ag_3PO_4/In_2S_3 composites show similar diffraction peaks as the pure In_2S_3, indicating that the In_2S_3 phase maintains well after the Ag_3PO_4 cocatalyst modification. Moreover, it should be noted that the diffraction peaks of In_2S_3 in Ag_3PO_4/In_2S_3 composites gradually weaken when the Ag_3PO_4 content increases, reflecting the decoration of more Ag_3PO_4 particles onto In_2S_3 surfaces. A similar phenomenon has also been observed in the Ag_3PO_4 moderated WS_2 sheets [23].

SEM was used to investigate the morphology and particle size of the as-prepared samples. As presented in Fig. 2a, pure In_2S_3 are uniform hierarchical microspheres with an average diameter of 5–6 μm and constructed by numerous interlaced two–dimensional nanosheets. The interlaced characteristic and/or assembly of the nanosheets produce abundant pores with size of 200–400 nm. Meanwhile, Ag_3PO_4 are composed of irregular agglomerate grains with size in the range of 300–900 nm (Fig. 2b). As for Ag_3PO_4/In_2S_3 composites with low mass ratio of Ag_3PO_4 loading, it can be clearly seen that small Ag_3PO_4 nanoparticles at size below 100 nm are uniformly and tightly anchored within the In_2S_3 porous surface, which indicates an intimate contact between Ag_3PO_4 and In_2S_3 (Fig. 2c). The reduced particle size of Ag_3PO_4 in composite might be due to the space–confined effect of In_2S_3 hierarchical pores [23]. However, when the mass ratio of Ag_3PO_4 increases, the Ag_3PO_4 nanoparticles are highly agglomerated and fulfill the porous surface of In_2S_3 (Fig. 2d), which largely reduces the contact area between these two materials and shields the incident light into In_2S_3 photocatalyst.

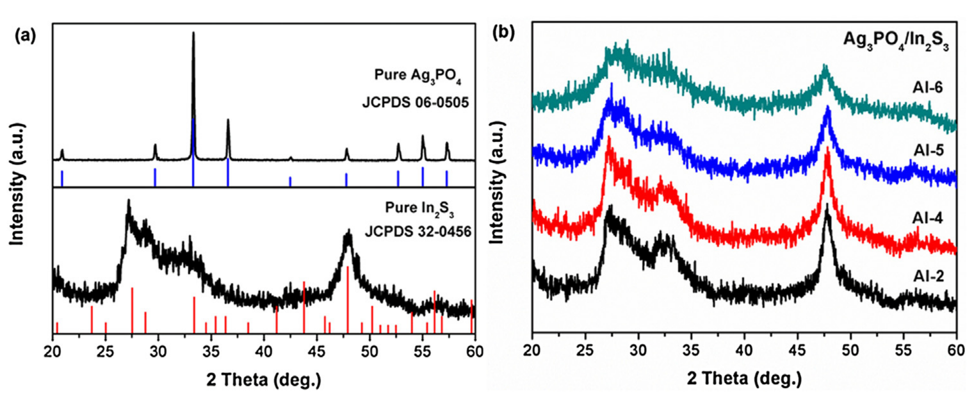

Fig 1. XRD patterns of (a) pure In_2S_3 and Ag_3PO_4, (b) Ag_3PO_4/In_2S_3 composites.

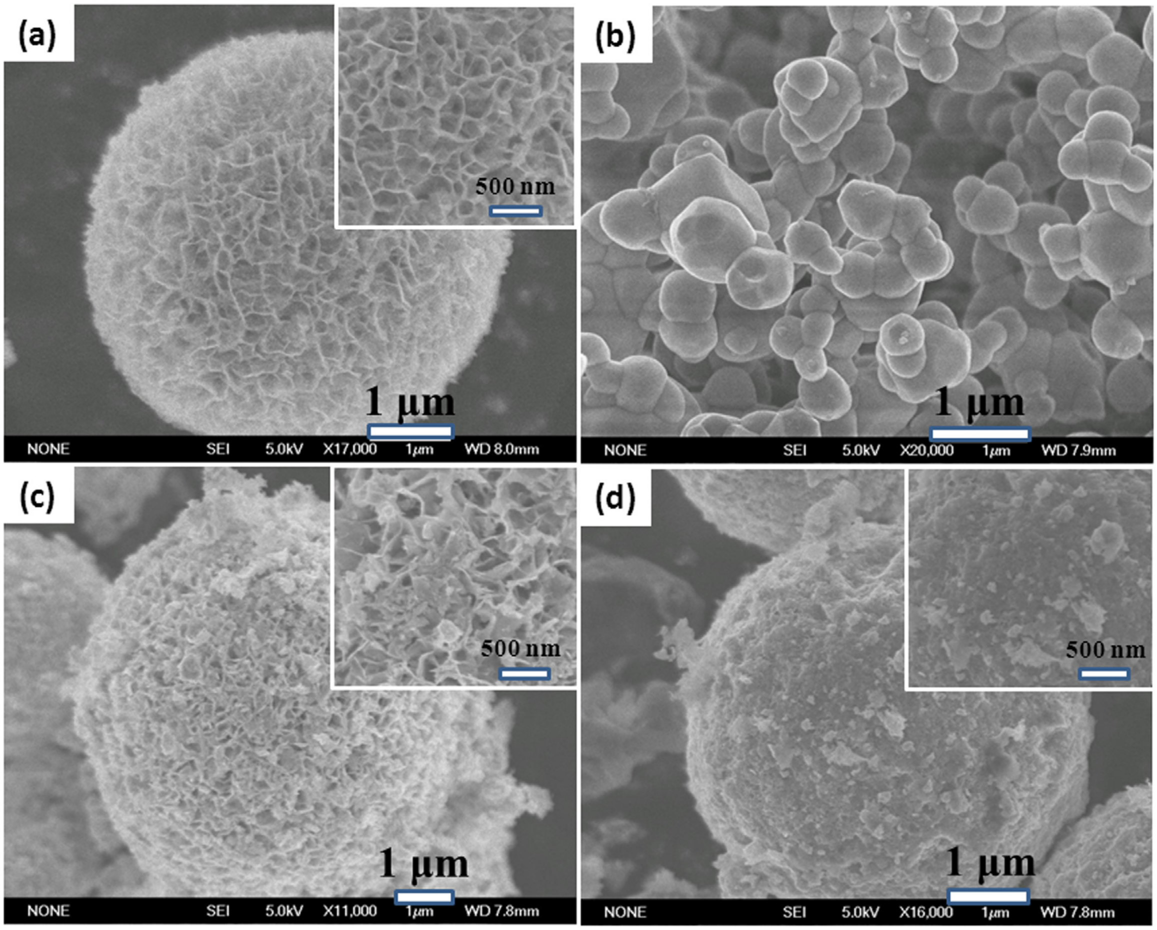

Fig. 2. SEM images of (a) pure In_2S_3, (b) pure Ag_3PO_4, and Ag_3PO_4/In_2S_3 composites: (c) AI–2 and (d) AI–6.

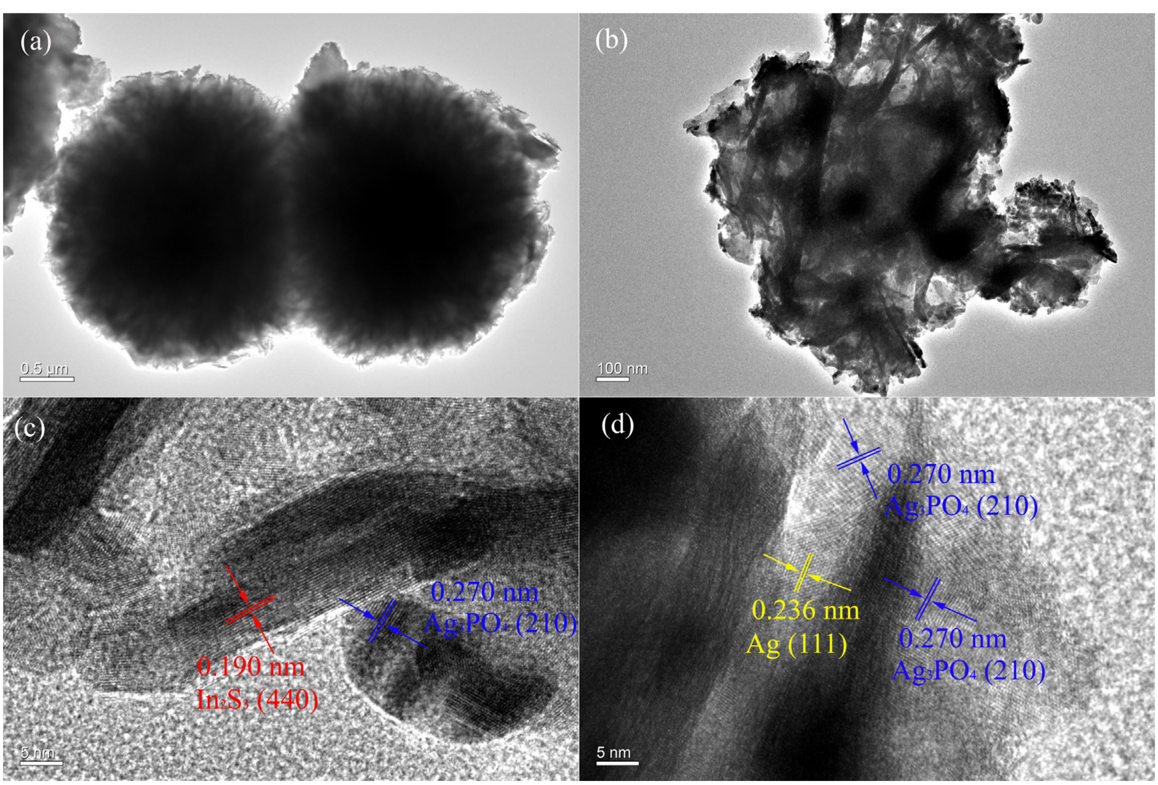

Fig. 3. (a, b) TEM and (c, d) HRTEM images of Ag_3PO_4/In_2S_3 composite (AI–2).

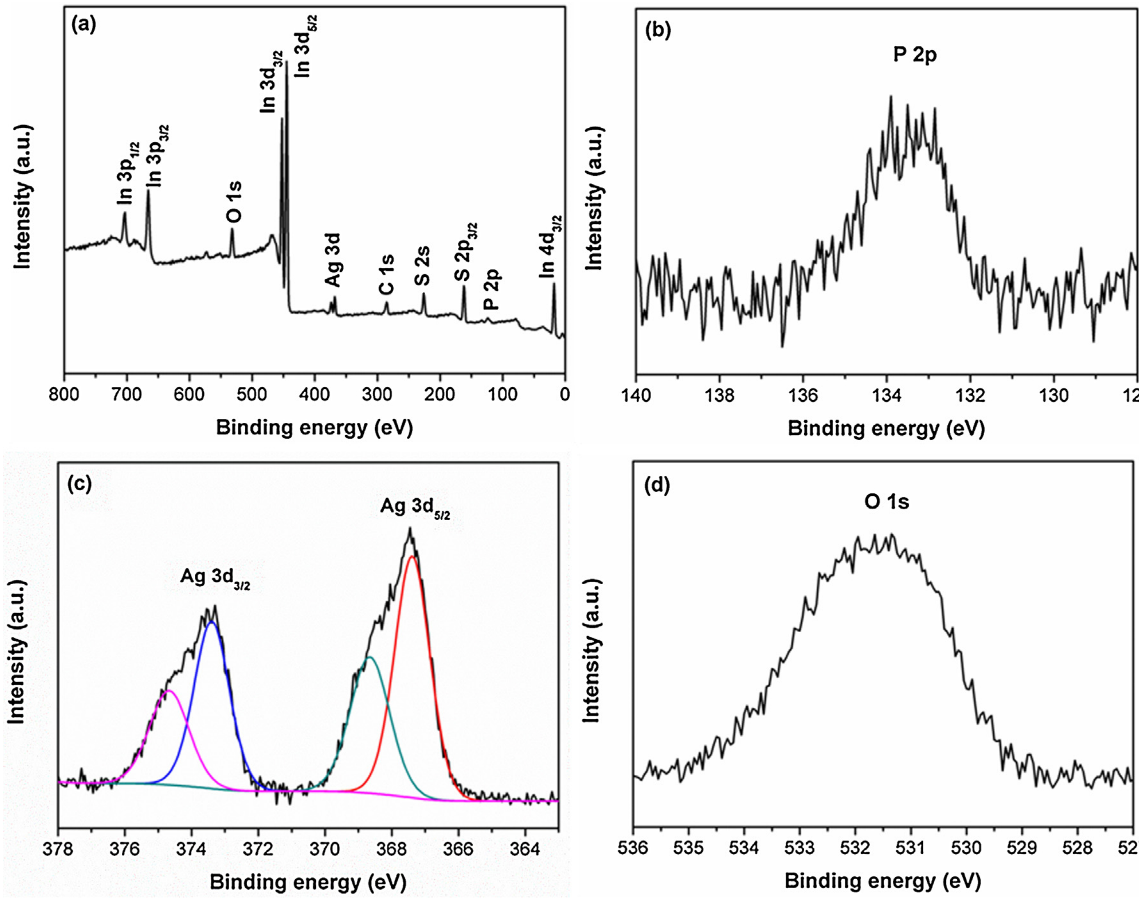

Fig. 4. (a) Wide scan spectrum of Ag_3PO_4/In_2S_3 composite (AI–2), and typical XPS spectra of (b) P 2p, (c) Ag 3d, (d) O 1s.

In order to ascertain the decoration of Ag_3PO_4 on the surface of In_2S_3, a typical Ag_3PO_4/In_2S_3 composite (AI–2) was selected and further investigated by TEM and HRTEM. Fig. 3a shows that the Ag_3PO_4/In_2S_3 composite is hierarchical microsphere consisting of numerous nanosheets, in accordance with the SEM results. On the scattered nanosheets in Fig. 3b, it can be clearly observed that many small nanoparticles with size < 20 nm are highly dispersed on the In_2S_3 nanosheets. Fig. 3c and d exhibit three kinds of lattice fringes in Ag_3PO_4/In_2S_3 composite. In specific, the fringe spacing of 0.270 nm is consistent with the (210) plane of Ag_3PO_4 component meanwhile that of 0.236 nm corresponds to the (111) lattice plane of metallic Ag, which suggests the coexistence of metallic Ag and Ag_3PO_4 in the composite. The fringe spacing of 0.19 nm matches well the (440) plane of cubic In_2S_3. Clear observation can find that two phases of In_2S_3 and Ag_3PO_4 closely contact to form an intimate interface, which favors the charge transfer between In_2S_3 and Ag_3PO_4 and may promote the separation of photogenerated electron-hole pairs.

The surface compositions and chemical states of Ag_3PO_4/In_2S_3 composite (AI–2) were further investigated by XPS. The full XPS spectrum (Fig. 4a) indicates that the Ag_3PO_4/In_2S_3 composite is composed of In, S, P, O and Ag elements. The XPS peak of C 1 s at 284.8 eV is assigned to residual carbon from the XPS instrument. The two strong peaks at 444.5 and 452.0 eV can be attributed to binding energies of In $3d_{5/2}$ and In $3d_{3/2}$, respectively (Fig. S3a, supporting information). The peak at 161.5 eV is assigned to the binding energy of the S 2p transition (Fig. S3b, supporting information). These values agree well with the reported data for In_2S_3 [30]. As observed from the high-resolution XPS spectrum in Fig. 4b, the P 2p peak is located at 133.4 eV, affirming that the valence state of P is +5. In the case of Ag 3d spectra (Fig. 4c), the strong peaks at 367.5 and 373.5 eV corresponding to Ag $3d_{5/2}$ and Ag $3d_{3/2}$ are characteristics of Ag^+, and the weak peaks at 368.9 and 374.9 eV can be ascribed to the Ag $3d_{5/2}$ and Ag $3d_{3/2}$ signals of metallic Ag [31,32], in consistent with the HRTEM result. The molar ratio of metallic Ag to Ag_3PO_4 in AI–2 calculated from Fig. 4c amounts to be 0.3. The binding energy of O 1 s in the composites is located at 531.3 eV (Fig. 4d), which is the feature of lattice oxygen.

The UV–vis DRS spectra of the Ag_3PO_4/In_2S_3 composites with different amount of Ag_3PO_4 modification are shown in Fig. 5. As

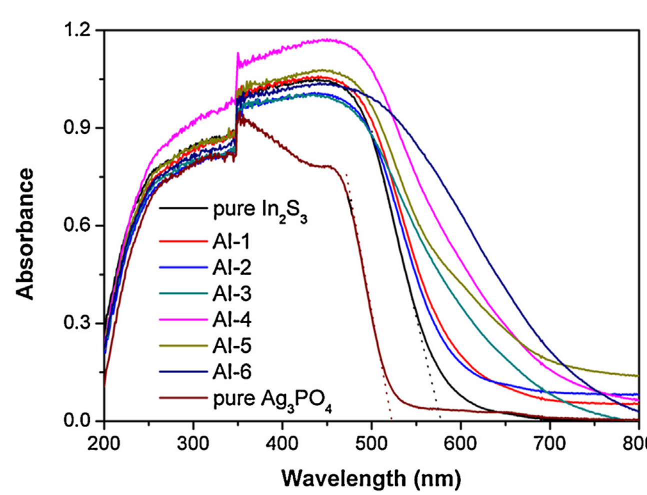

Fig. 5. UV–vis DRS spectra of pure In_2S_3, Ag_3PO_4 and Ag_3PO_4/In_2S_3 composites.

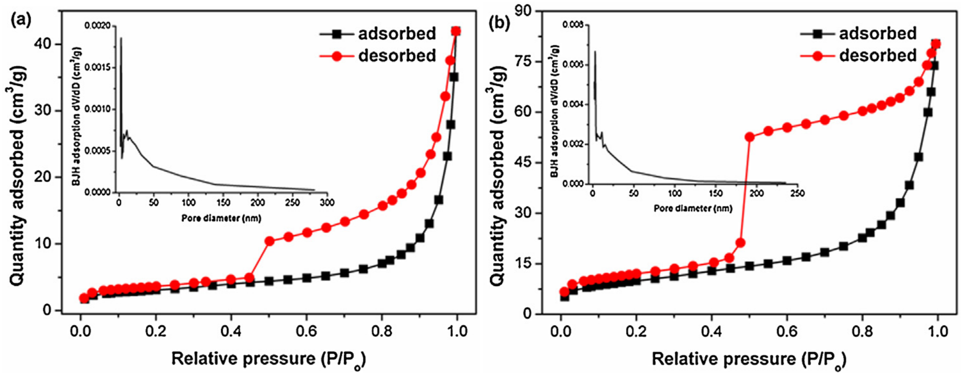

Fig. 6. N_2 sorption isotherms and pore size distributions of pure In_2S_3 (a) and Ag_3PO_4/In_2S_3 composite (AI–2).

can be seen, pure In_2S_3 sample performs a 577 nm absorption band-edge in the visible region, corresponding to a band gap energy of 2.15 eV, which is much larger than that of the bulk material (2.0 eV). The blue-shift of optical absorption for the present In_2S_3 microspheres can be attributed to the strong quantum confinement of the excitonic transition for sheetlike structures [4,29]. The pure Ag_3PO_4 shows a sharp fundamental absorption edge at about 520 nm, well consistent with other studies [16,32,33]. As compared, the absorption edge of Ag_3PO_4/In_2S_3 composites is gradually right-shift to long wavelength with increased Ag_3PO_4 content, which in turn promotes the utilization efficiency of solar light and will benefit the photocatalytic activity. In addition, it should be noted that the Ag_3PO_4/In_2S_3 composites also show light absorption in the region of 600–800 nm, which is attributed to the plasmonic effect of Ag nanoparticles [19,34].

Fig. 6 shows the N_2 adsorption/desorption isotherms and the corresponding pore size distribution plots for pure In_2S_3 and Ag_3PO_4/In_2S_3 composite (AI–2). According to the Brunauer–Deming–Deming–Teller (BDDT) classification, pure In_2S_3 microspheres display a type–IV isotherm with a hysteresis loop in the range of 0.45–0.95 P/P_0 (Fig. 6a), implying the presence of mesopores. Insert of Fig. 6a shows that the In_2S_3 microspheres have a wide pore size distribution, ranging from 2 to 250 nm, as calculated from desorption branch of N_2 isotherm by Barrett–Joyner–Halenda (BJH) method. BET surface area of pure In_2S_3 is about 10.7 $m^2 \cdot g^{-1}$. In comparison with In_2S_3, the porosity of AI–2 apparently increases when trace amount (0.086 wt%) of Ag_3PO_4 nanoparticles were introduced, as evident by the increase in volume adsorbed at high pressure (Fig. 6b). The pore-size distribution plot in Fig. 6b shows that the composite exhibits a pore size distribution in the range of 2 to 150 nm. This narrow pore size distribution should be due to the decoration of small Ag_3PO_4 nanoparticles within the interlaced nanosheets of In_2S_3. The decoration of Ag_3PO_4 nanoparticles within In_2S_3 hierarchical microspheres dramatically increases the surface area to 35.2 $m^2\,g^{-1}$, providing more active sites to adsorb the organic pollutants and to degrade them. However, after more Ag_3PO_4 nanoparticles were introduced, the porous surface of In_2S_3 is fulfilled and a smooth surface is observed (Fig. 2d), resulting in decreased surface areas. The BET surface area of Ag_3PO_4/In_2S_3 composites with various compositions is shown in Table 1.

3.2. Photocatalytic activity

Photocatalytic activity was firstly evaluated by photodegradation of methyl orange (MO, anionic dye) in aqueous solution under visible light irradiation. Prior to irradiation, the adsorption behaviour was initially examined under dark condition. The adsorption–desorption balance was achieved between the photocatalysts and MO under intense stirring after 1 h. Fig. 7a shows the temporal evolution of the spectral changes of MO mediated by various photocatalysts in dark. Pure In_2S_3 displays a weak adsorption capability for MO (less than 10%). As compared, most of the Ag_3PO_4/In_2S_3 composites (AI–1, AI–2, AI–3 and AI–4) exhibit an increase of 4~5 times for MO adsorption. However, a high amount of Ag_3PO_4 modification (AI–5 and AI–6) induces poor adsorption capability. This adsorption trend is consistent with the change of surface area. The adsorption amount of MO over photocatalysts is shown in Fig. 7b. Since the adsorption capacity has a significant effect on the degradation behaviour for organic pollutants, the Ag_3PO_4/In_2S_3 composites with superior adsorption capability are expected to exhibit high photocatalytic degradation ability towards the target contaminants.

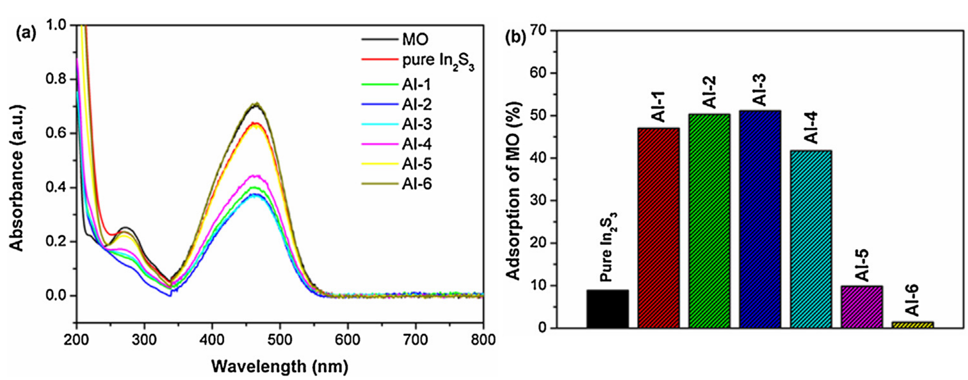

Fig. 7. The adsorption behaviour of various photocatalysts for MO under dark conditions: (a) the temporal evolution of the spectral changes of MO and (b) the adsorption amount of MO.

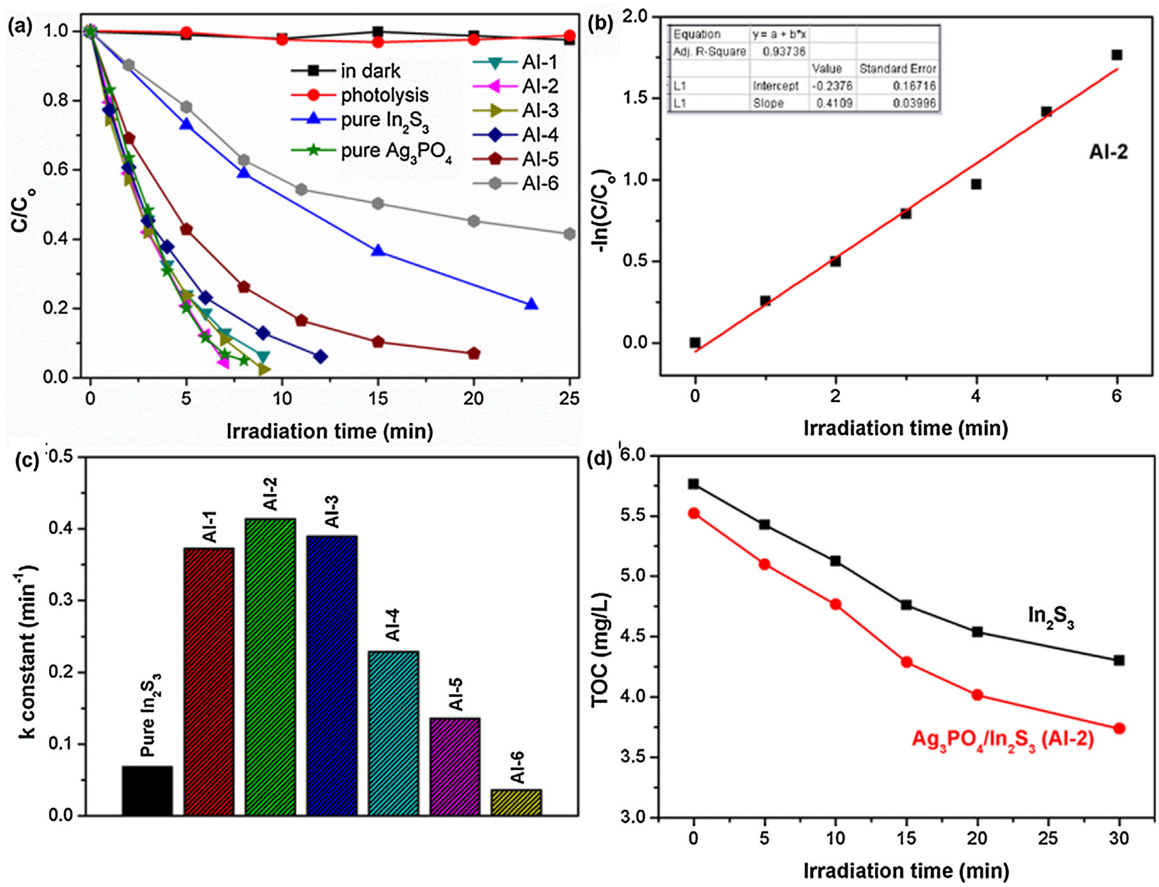

Fig. 8. (a) Photocatalytic degradation curves of MO over pure In_2S_3 and Ag_3PO_4/In_2S_3 composites, (b) the kinetic of MO photocatalytic degradation over Ag_3PO_4/In_2S_3 composite (AI–2), (c) the kinetic constants of MO degradation by various photocatalysts, and (d) changes in TOC during the course of photocatalytic degradation of MO in the presence of pure In_2S_3 and Ag_3PO_4/In_2S_3 (AI–2).

Fig. 8a shows the photocatalytic activity of pure In_2S_3, Ag_3PO_4 and Ag_3PO_4/In_2S_3 composites under visible light irradiation. The photolysis of MO in the absence of photocatalysts is negligible within the test period as MO molecule is quite stable under visible light illumination. No decomposition of MO is observed in the presence of catalyst in dark condition, showing the importance of light irradiation. Pure In_2S_3 can degrade 80% of MO after irradiation of 25 min. However, the activity of Ag_3PO_4/In_2S_3 composites is significantly enhanced and found to be a function of the Ag_3PO_4 content. The photocatalytic activity of AI–2 exceeds all other samples by far: MO is completely degraded after only irradiation of 7 min, even comparable to that of the highly efficient Ag_3PO_4 sample. The photodegradation curves of MO are fitted by pseudo–first–order reaction kinetics, and the kinetic plots over AI–2 are shown in Fig. 8b. The rate constants of all samples are given in Fig. 8c. Clearly, the majority of the Ag_3PO_4/In_2S_3 composites degrade MO at higher rates than pure In_2S_3. The highest rate constant of AI–2 is ~6 times higher than that of In_2S_3. The variation of the rate constants is consistent with the variation in photocatalytic activity, as the rate constants first increases and then decreases with the increased Ag_3PO_4 content.

To further evaluate the degree of degradation or mineralization of MO dye, the TOC experiment was performed. The comparative results of TOC measurements (Fig. 8d) before and after photocatalytic reaction show that the mineralization yield of AI–2 reaches a value of 32.3% after 30 min of irradiation, while that of pure In_2S_3 is 25.4% after the same period of irradiation. The discrepancy between mineralization yield and degradation of dye may be due to the fact that the mineralization of the dye usually processes through two steps, namely, the ring cleavage and subsequently the oxidation of the fragments [37].

The stability of a photocatalyst is also an important issue for its assessment and application. The sulfide photocatalysts have been reported to lose frequently activity during photocatalytic reaction due to corrosion accompanied by dissolution of the solid [35]. In_2S_3 is shown to be more active and photocorrsion resistant than CdS [36]. In order to study the lifespan and stability of AI-2 during MO

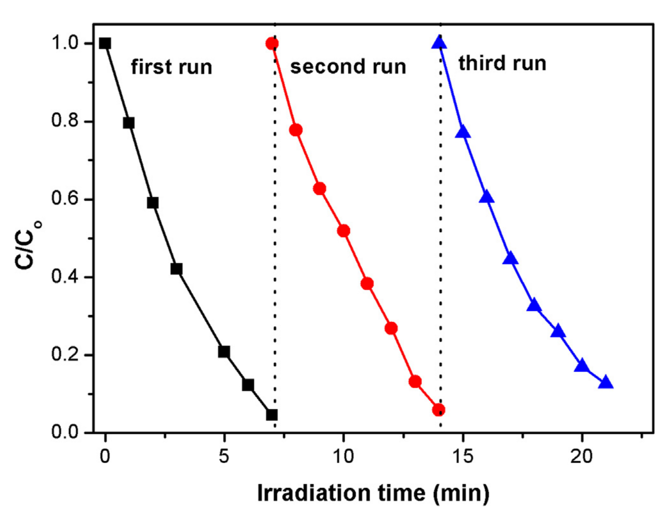

Fig. 9. Cycling runs for MO degradation in the presence of Ag_3PO_4/In_2S_3 composite (AI–2).

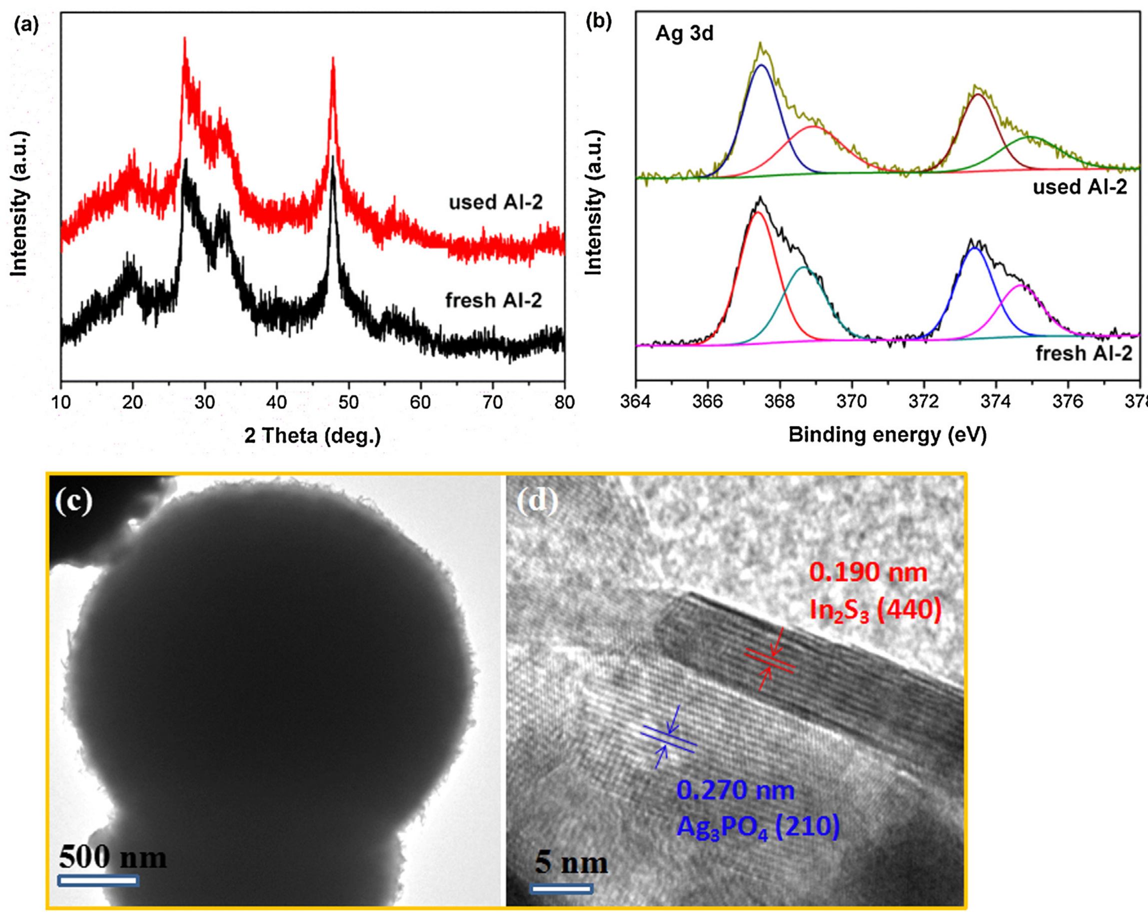

Fig. 10. (a) XRD and (b) Ag 3d XPS spectra of Ag_3PO_4/In_2S_3 (AI–2) before and after photocatalytic reaction; (c) TEM and (d) HRTEM images of Ag_3PO_4/In_2S_3 (AI–2) after photocatalytic reaction.

degradation, recycled experiments were performed, and the results are displayed in Fig. 9. The activity of AI-2 reaches 98% after one cycle (7 min) and remains at above 90% throughout three cycles, indicating that Ag_3PO_4/In_2S_3 composite acts as a stable photocatalyst. Fig. 10a exhibits the XRD patterns of AI-2 before and after three recycling runs of MO degradation. No evident crystalline structure changes can be observed in the XRD pattern. The result is also confirmed by TEM and HRTEM images (Fig. 10c, d) of the composite after reaction, which clearly show the well sphere–like structure and clear lattice planes for In_2S_3 and Ag_3PO_4. To further evaluate the surface component and composition of AI–2, the compared Ag 3d XPS spectra before and after photocatalytic reaction are given in Fig. 10b. Similar to the fresh sample, the used AI–2 displays characteristic peaks attributing to metallic Ag (at 369.0 and 375.0 eV) and Ag^+ in Ag_3PO_4 (at 367.6 and 373.6 eV). According to XPS calculation analysis, the content of metallic Ag in the used sample shows no obvious increase (0.305) as compared to that in the fresh sample (0.3). Therefore, the decoration of Ag_3PO_4 onto In_2S_3 can not only enhance the photocatalytic performance of In_2S_3, but also inhibit the photocorrsion and therefore, promote the stable-durability of its photocatalytic activity.

Ag_3PO_4/In_2S_3 composites also exhibited excellent photocatalytic performance towards the removal of cationic dyes (such as MB and RhB) and colorless chemical pollutants (such as phenol and salicylic acid) under visible light irradiation. Fig. 11 show the adsorption capacity and degradation results of various organic pollutants over AI–2 and pure In_2S_3. As can be seen, AI–2 exhibits much stronger adsorption capacity for MB and RhB than phenol and salicylic acid. The weaker adsorption of phenol than MB dye has also been observed over PANI/C_3N_4 nanosheets [38]. After irradiation of 5 min, both RhB and MB solutions are almost colorless in the presence of AI–2, while the complete decolonization of these dyes by pure In_2S_3 needs 15 min. Since phenol and salicylic acid are not so easy to be adsorbed, the removal rates of them over AI–2 are relatively low, and after 3 h of irradiation, the degradation ratio is about 53% and 62%, respectively. The above results show that Ag_3PO_4/In_2S_3 composite photocatalysts have no–selectivity and can effectively degrade different kinds of organic pollutants.

Modifying the photocatalysts with some essential noble metal, such as Pt, Pd or Ru is an alternative way to improve the photocatalytic performance as these ingredients can serve as co–catalysts to improve the trapping efficiency of photoinduced electrons and reduce the kinetic activation barrier due to their large work function [39]. For comparison, the photocatalytic performance of Pt/In_2S_3 was also investigated under the identical experimental conditions. The result in Fig. S4 shows that Pt/In_2S_3 exhibits comparable adsorption capacity to that of Ag_3PO_4/In_2S_3 composite but poor photocatalytic activity. This confirms that the activity enhancement on In_2S_3 can be achieved by loading Ag_3PO_4, which plays the similar cocatalytic role as noble metal during photocatalysis. Moreover, when the same amount of Ag_3PO_4 was coated on Al_2O_3 particles, the prepared Ag_3PO_4/Al_2O_3 composite displays negligible photocatalytic performance towards MO degradation, suggesting the active role of support material during photocatalytic reaction.

In addition, a similar $Ag_3PO_4/ZnIn_2S_4$ system has also been fabricated. The SEM images show that the Ag_3PO_4 nanoparticles have been well anchored within the porous surface of

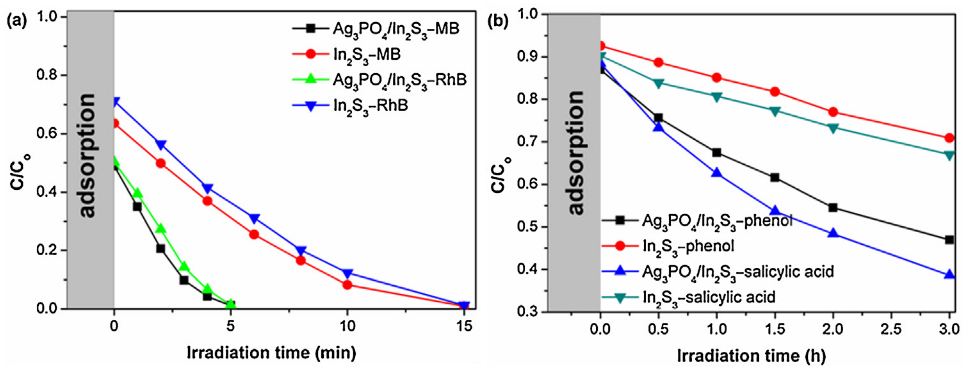

Fig. 11. Compared photocatalytic activities towards degradation of (a) MB and RhB, and (b) phenol and salicylic acid under visible light irradiation over pure In_2S_3 and Ag_3PO_4/In_2S_3 (AI–2).

hierarchical $ZnIn_2S_4$ microspheres (Fig. S5, supporting information). Similar trends of adsorption and photocatalytic activity over $Ag_3PO_4/ZnIn_2S_4$ composites are observed as that over Ag_3PO_4/In_2S_3 composites (Fig. S6, supporting information). These results indicate that Ag_3PO_4 can act as cocatalyst to improve the photocatalytic performance of binary sulfides or ternary chalcogenides photocatalysts.

3.3. Possible photocatalytic mechanism

The possible photodegradation mechanism was investigated by performing the radical–trapping experiments with different scavengers. The results in Fig. 12a show that the addition of TBA and AO has no effect on the photocatalytic activity of Ag_3PO_4/In_2S_3 while the introduction of BQ obviously inhibits the activity. This indicates that $^{\bullet}O_2^-$ are the main reactive species for the degradation of MO over Ag_3PO_4/In_2S_3 composites. The presence of $^{\bullet}O_2^-$ radicals was further proved by a nitroblue tetrazolium (NBT) probe method [40]. Fig. 12b shows that the maximum absorption peak at 259 nm decreases with the prolonging irradiation time, indicating the specific reaction between NBT and $^{\bullet}O_2^-$ radicals. The above results demonstrate that the photodegradation of organic pollutants over Ag_3PO_4/In_2S_3 composites is mainly dominated by the oxidation action of the generated $^{\bullet}O_2^-$ radicals.

In order to fully understand the photocatalytic mechanism of Ag_3PO_4/In_2S_3 composites, the band–edge potentials of CB and VB, designated as E_{CB} and E_{VB}, can be calculated from the following equation [41]:

$$E_{VB} = X - E_0 + 1/2E_g$$

$$E_{CB} = X - E_0 - 1/2E_g$$

in which X is the absolute electronegativity of the semiconductor, determined by the geometric mean of the absolute electronegativity of constituent atoms, which is defined as the arithmetic mean of the atomic electron affinity and the first ionization energy; E_0 is the energy of free electrons on the hydrogen scale (about 4.5 eV); and E_g is the band gap of the semiconductor. E_{CB} and E_{VB} of Ag_3PO_4 are determined to be 0.25 and 2.67 eV, while those of In_2S_3 are −1.04 and 1.44 eV. On the basis of the alignment of their energy levels, an illustration of possible interface electron transfer behavior is proposed and shown in Fig. 13. Because Ag nanoparticles are also formed in the composite, the metal Ag should show its contribution in separation of electron−hole pairs [42–44]. If the photoexcited charge carriers transfer in the Ag_3PO_4/In_2S_3 composite according to Fig. 13a, which is the common electron–hole separation process for a great number of composite photocatalysts, the photoexcited electrons in the CB of In_2S_3 would transfer to that of Ag_3PO_4 and then metallic Ag, while the photoexcited holes accumulate on the VB of In_2S_3. In this manner, the electron and holes are efficiently separated. However, the accumulated electrons in metallic Ag can not reduce O_2 to yield $^{\bullet}O_2^-$ because the CB edge potential of Ag_3PO_4 (0.25 eV vs. NHE) is more positive than that of $O_2/^{\bullet}O_2^-$ (−0.33 eV vs. NHE). Therefore, if the Ag_3PO_4/In_2S_3 composites follow the traditional model (Fig. 12a), the introduction of Ag_3PO_4 to In_2S_3 is not favorable for the generation of the main reactive species ($^{\bullet}O_2^-$) and does not significantly promote organic pollutants degradation. More recently, many scientists reported some efficient composite photocatalysts such as Ag_3PO_4/AgI, Ag_3PO_4/g-C_3N_4 and so on, believed to follow a Z−scheme mechanism [45–47], which inspires

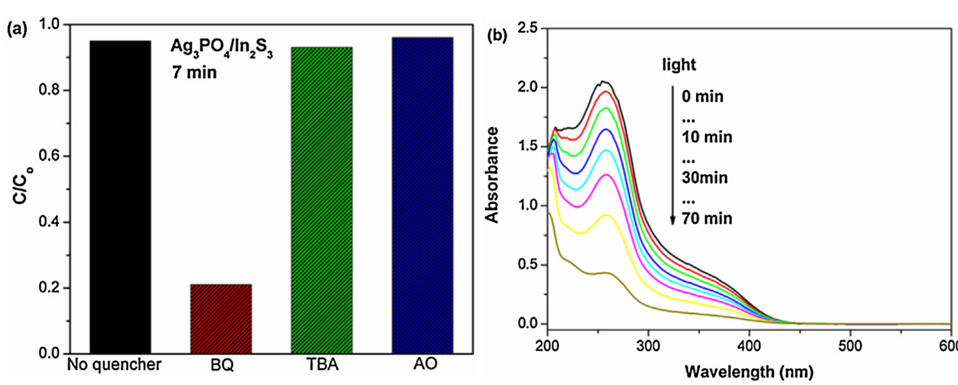

Fig. 12. (a) Effects of scavengers on the degradation efficiency of MO over Ag_3PO_4/In_2S_3 composite (AI–2), (b) UV–vis absorption spectra of NBT in Ag_3PO_4/In_2S_3 composite (AI–2) suspension under visible light irradiation.

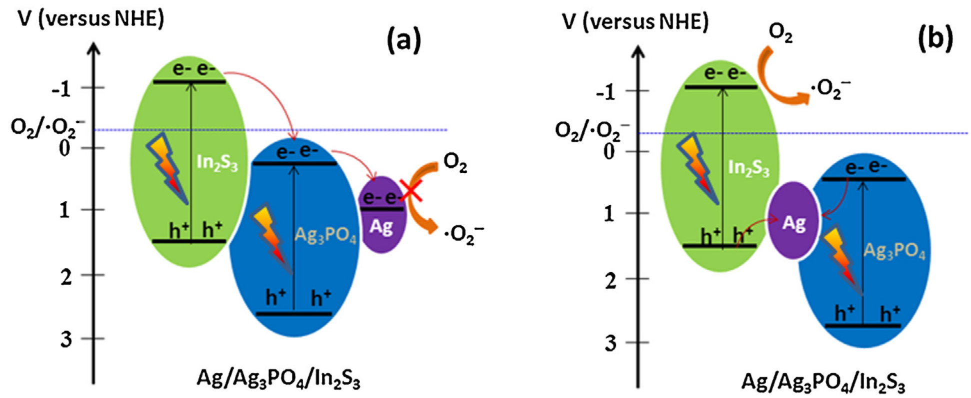

Fig. 13. Schematic diagram of photoexcited electron–hole separation processes of the Ag_3PO_4/In_2S_3 composites: (a) traditional model and (b) Z – scheme mechanism.

us to believe that the Z–scheme mechanism might also work in the Ag_3PO_4/In_2S_3 composite photocatalysts. As shown in Fig. 13b, Ag nanoparticles may act as a charge transmission bridge to form the $Ag_3PO_4/Ag/In_2S_3$ Z – scheme system. Due to the CB edge of Ag_3PO_4 is more negative than the Fermi level of metallic Ag, the photogenerated electrons in the CB of Ag_3PO_4 shift to metallic Ag. Simultaneously, the holes in the VB of In_2S_3 move to metallic Ag and combine with the electrons. This type of charge transmission efficiently enhances the separation of electron–hole pairs and enables the electrons and holes to remain on the CB of In_2S_3 and VB of Ag_3PO_4, respectively, contributing to the structural stability for both In_2S_3 and Ag_3PO_4.

The strong charge separation and migration capacity of $Ag_3PO_4/Ag/In_2S_3$ can be proved by the enhanced photocurrent under visible light irradiation. Fig. 14a show the photocurrent measured for pure In_2S_3 and AI–2 as a function of time at zero bias voltage with light – on and light – off cycles. As expected, AI–2 shows two times larger photocurrent than In_2S_3. Fig. 14b indicate the EIS Nyquist plots of pure In_2S_3 and AI – 2. It can be seen that the arc radius on EIS Nyquist plot of AI–2 film is smaller than that of In_2S_3, which means a fast interfacial charge–transfer process and effective separation of photogenerated electron–hole pairs. The PL emission spectra are also used to survey the separation efficiency of the photogenerated electron–hole pairs in a semiconductor. Generally, the lower the PL intensity, the smaller probability the photogenerated electron–hole pairs recombination [48]. Fig. 14c illustrate the PL spectra of In_2S_3 and AI–2. The PL emission intensity of AI–2 is dramatically weakened compared with that of In_2S_3, indicating the restrain of the recombination of photogenerated charge carriers by the introduction of Ag_3PO_4. The results of PL, photocurrent and EIS are well consistent and indicate that the loading of ultra–low amount of Ag_3PO_4 can remarkably enhance the separation efficiency and interfacial charge transfer efficiency of photogenerated electron–hole pairs in In_2S_3.

The above characterization results and proposed mechanism imply that Ag–Ag_3PO_4 can serve as efficient cocatalyst to promote charge separation by capturing photogenerated holes in In_2S_3 photocatalyst, contributing to an improved photocatalytic activity and stability. Moreover, decoration of trace amount of Ag_3PO_4 nanoparticles within porous In_2S_3 microspheres gives more active

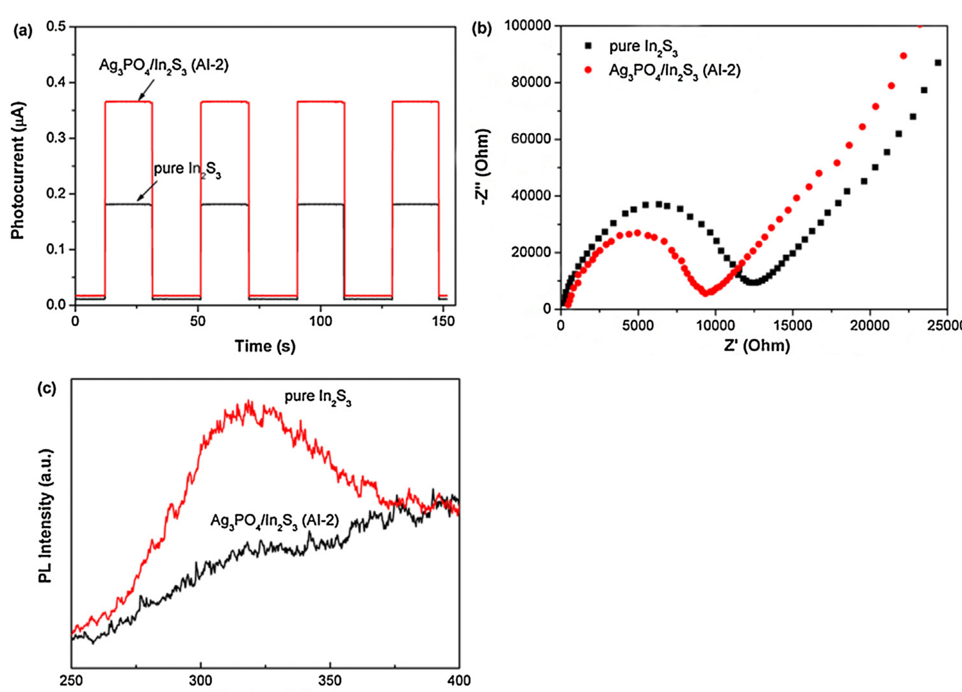

Fig. 14. (a) Transient photocurrent response, (b) Electrochemical impedance spectroscopy, and (c) PL spectra of pure In_2S_3 and Ag_3PO_4/In_2S_3 composite (AI – 2).

sites for organic pollutants adsorption and oxidation due to the larger surface area (Table 1). However, the introduction of more Ag_3PO_4 nanoparticles results in less effective contact between Ag_3PO_4 nanoparticles and In_2S_3 nanosheets, leading to the weak interfacial charge transfer, which as a consequence will decrease the photocatalytic activity.

4. Conclusions

$Ag-Ag_3PO_4$ is demonstrated to be new and efficient cocatalyst to improve the photocatalytic performance of In_2S_3 and $ZnIn_2S_4$ photocatalysts even at an ultra–low loading level. After decoration of Ag_3PO_4 nanoparticles, the Ag_3PO_4/In_2S_3 composite photocatalysts exhibit excellent photocatalytic activity and stability for organic pollutants degradation. Compared with traditional cocatalysts like noble metal and graphene acting as acceptors for photogenerated electrons, the $Ag–Ag_3PO_4$ can capture photogenerated holes from In_2S_3 by a Z–scheme mechanism. In the $Ag_3PO_4/Ag/In_2S_3$ system, Ag nanoparticles function as the charge transmission bridge to capture photogenerated electrons in Ag_3PO_4 and photogenerated holes in In_2S_3, remaining the strong reducibility of electrons in In_2S_3 CB and inhibiting the photocorrsion of In_2S_3. The current work may give ideas for the application of Ag_3PO_4 as cocatalyst and fabrication of other efficient composite photocatalysts, which can be used to remove harmful organic dyes in wastewater.

Acknowledgments

This work was financially supported by a research Grant from the National Basic Research Program of China (No. 2013CB632401), the National Natural Science Foundation of China (no. 21103193, 21275089, and 21303094), Doctoral Foundation of Shandong Province (BS2013NJ013), China Postdoctoral Science Foundation (2015M572011), National Undergraduate Training Program for Innovation and Entrepreneurship (201510446061), and Taishan Scholar Foundation of Shandong Province, China.

Appendix A. Supplementary data

Supplementary data associated with this article can be found, in the online version, at http://dx.doi.org/10.1016/j.apcatb.2016.09.017.

References

[1] J.H. Yang, D.G. Wang, H.X. Han, C. Li, Acc. Chem. Res. 46 (2013) 1900–1909.
[2] J.R. Ran, J. Zhang, J.G. Yu, M. Jaroniec, S.Z. Qiao, Chem. Soc. Rev. 43 (2014) 7787–7812.
[3] D.W. Jing, L.J. Guo, J. Phys. Chem. B 110 (2006) 11139–11145.
[4] Y.H. He, D.Z. Li, G.C. Xiao, W. Chen, Y.B. Chen, M. Sun, H.J. Huang, X.Z. Fu, J. Phys. Chem. C 113 (2009) 5254–5262.
[5] Y.Q. Lei, S.Y. Song, W.Q. Fan, Y. Xing, H.J. Zhang, J. Phys. Chem. C 113 (2009) 1280–1285.
[6] Y. Liu, Y.H. Deng, Z.K. Sun, J. Wei, G.F. Zheng, A.M. Asiri, S.B. Khan, M.M. Rahman, D.Y. Zhao, Small 9 (2013) 2702–2708.
[7] Z.B. Lei, W.S. You, M.Y. Liu, G.H. Zhou, T. Takata, M. Hara, K. Domen, C. Li, Chem. Commun. 17 (2003) 2142–2143.
[8] B.B. Kale, J.O. Baeg, S.M. Lee, H. Chang, S.J. Moon, C.W. Lee, Adv. Funct. Mater. 16 (2006) 1349–1354.
[9] T.J. Yan, L.P. Li, G.S. Li, Y.J. Wang, W.B. Hu, X.F. Guan, J. Hazard. Mater. 186 (2011) 272–279.
[10] X. Zong, H. Yan, G. Wu, G. Ma, F. Wen, L. Wang, C. Li, J. Am. Chem. Soc. 130 (2008) 7176–7177.
[11] X. Zong, J. Han, G. Ma, H. Yan, G. Wu, C. Li, J. Phys. Chem. C 115 (2011) 12202–12208.
[12] S.H. Shen, X.B. Chen, F. Ren, C.X. Kronawitter, S.S. Mao, L.J. Guo, Nanoscale Res. Lett. 6 (2011) 290–295.
[13] L.J. Zhang, R. Zheng, S. Li, B.K. Liu, D.J. Wang, L.L. Wang, T.F. Xie, ACS Appl. Mater. Interfaces 6 (2014) 13406–13412.
[14] L. Ye, J.L. Fu, Z. Xu, R.S. Yuan, Z.H. Li, ACS Appl. Mater. Interfaces 6 (2014) 3483–3490.
[15] Y. Wang, Q. Wang, X. Zhan, F. Wang, M. Safdar, J. He, Nanoscale 5 (2013) 8326–8339.
[16] Z.G. Yi, J.H. Ye, N. Kikugawa, T. Kako, S.X. Ouyang, H. Stuart-Williams, H. Yang, J.Y. Cao, W.J. Luo, Z.S. Li, Y. Liu, R.L. Withers, Nat. Mater. 9 (2010) 559–564.
[17] J.J. Guo, S.X. Ouyang, H. Zhou, T. Kako, J.H. Ye, J. Phys. Chem. C 117 (2013) 17716–17724.
[18] Y.P. Bi, S.X. Ouyang, J.Y. Cao, J.H. Ye, Phys. Chem. Chem. Phys. 13 (2011) 10071–10075.
[19] X.J. Guan, L.J. Guo, ACS Catal. 4 (2014) 3020–3026.
[20] W.F. Yao, B. Zhang, C.P. Huang, C. Ma, X.L. Song, Q.J. Xu, J. Mater. Chem. 22 (2012) 4050–4055.
[21] S. Kumar, T. Surendar, A. Baruah, V. Shanker, J. Mater. Chem. A 1 (2013) 5333–5340.
[22] L. Liu, Y.H. Qi, J.R. Lu, S.L. Lin, W.J. An, Y.H. Liang, W.Q. Cui, Appl. Catal. B: Environ. 183 (2016) 133–141.
[23] H.J. Yu, Y. Yu, J.H. Liu, P.Y. Ma, Y.C. Wang, F. Zhang, Z.Y. Fu, J. Mater. Chem. A 3 (2015) 19439–19444.
[24] C.S. Zhu, L. Zhang, B. Jiang, J.T. Zheng, P. Hu, S.J. Li, M.B. Wu, W.T. Wu, Appl. Surf. Sci. 377 (2016) 99–108.
[25] X. Lin, X.Y. Guo, W.L. Shi, F. Guo, G.B. Che, H.J. Zhai, Y.S. Yan, Q.W. Wang, Catal. Commun. 71 (2015) 21–27.
[26] T.J. Yan, W.F. Guan, W.J. Li, J.M. You, RSC Adv. 4 (2014) 37095–37099.
[27] Y.L. Min, X.F. Qi, Q.J. Xu, Y.C. Chen, CrystEngComm 16 (2014) 1287–1295.
[28] L.Q. Jing, Y. Cao, H.Q. Cui, J.R. Durrant, J.W. Tang, D.N. Liu, H.G. Fu, Chem. Commun. 48 (2012) 10775–10777.
[29] L.Y. Chen, Z.D. Zhang, W.Z. Wang, J. Phys. Chem. C 112 (2008) 4117–4123.
[30] F. Teng, Z.L. Liu, A. Zhang, M. Li, Environ. Sci. Technol. 49 (2015) 9489–9494.
[31] T.J. Yan, H.W. Zhang, Q. Luo, Y.Y. Ma, H.X. Lin, J.M. You, Chem. Eng. J. 32 (2013) 564–572.
[32] Y.P. Bi, S.X. Ouyang, N. Umerzawa, J.Y. Cao, J.H. Ye, J. Am. Chem. Soc. 133 (2011) 6490–6492.
[33] T.J. Yan, G.F. Guan, J. Tian, P. Wang, W.J. Li, J.M. You, B.B. Huang, J. Alloys Compd. 680 (2016) 436–445.
[34] Y.P. Bi, H.Y. Hu, S.X. Ouyang, Z.B. Jiao, G.X. Lu, J.H. Ye, Chem. Eur. J. 18 (2012) 14272–14275.
[35] Z.B. Lei, W.S. You, M.Y. Liu, G.H. Zhou, T. Takata, M. Hara, K. Domen, C. Li, Chem. Commun. (2003) 2142–2143.
[36] R. Lucena, F. Fresno, J.C. Conesa, Catal. Commun. 20 (2012) 1–5.
[37] C.S. Pan, Y.F. Zhu, Environ. Sci. Technol. 44 (2010) 5570–5574.
[38] W.J. Jiang, W.J. Luo, R.L. Zong, W.Q. Yao, Z.P. Li, Y.F. Zhu, Small (2016), http://dx.doi.org/10.1002/smll.201601546.
[39] L. Zhang, X.L. Fu, S.G. Meng, X.L. Jiang, J.H. Wang, S.F. Che, J. Mater. Chem. A 3 (2015) 23732–23742.
[40] T.J. Yan, W.F. Guan, L.T. Cui, Y.Q. Xu, J. Tian, RSC Adv. 5 (2015) 43756–53764.
[41] S.F. Chen, L. Ji, W.M. Tang, X.L. Fu, Dalton Trans. 42 (2013) 10759–10768.
[42] P. Wang, B.B. Huang, X.Y. Qin, X.Y. Zhang, Y. Dai, J.Y. Wei, M.H. Whangbo, Angew. Chem. Int. Ed. 47 (2008) 7931–7933.
[43] T. Hirakawa, P.V. Kamat, J. Am. Chem. Soc. 127 (2005) 3928–3934.
[44] J. Zhang, L.P. Li, T.J. Yan, G.S. Li, J. Phys. Chem. C 115 (2011) 13820–13828.
[45] L.Q. Ye, J.Y. Liu, C.Q. Gong, L.H. Tian, T.Y. Peng, L. Zan, ACS Catal. 2 (2012) 1677–1683.
[46] X.F. Wang, S.F. Li, Y.Q. Ma, H.G. Yu, J.G. Yu, J. Phys. Chem. C 115 (2011) 14648–14655.
[47] Y.M. He, L.H. Zhang, B.T. Teng, M.H. Fan, Environ. Sci. Technol. 49 (2015) 649–656.
[48] J. Di, J.X. Xia, Y.P. Ge, H.P. Li, H.Y. Ji, H. Xu, Q. Zheng, H.M. Li, M.N. Li, Appl. Catal. B: Environ. 168 (2015) 51–61.